Cell Reports
Physical Science

Article

Combining μ-MRI with cellular automata simulation for an improved insight into cell growth within scaffolds

Graphical abstract

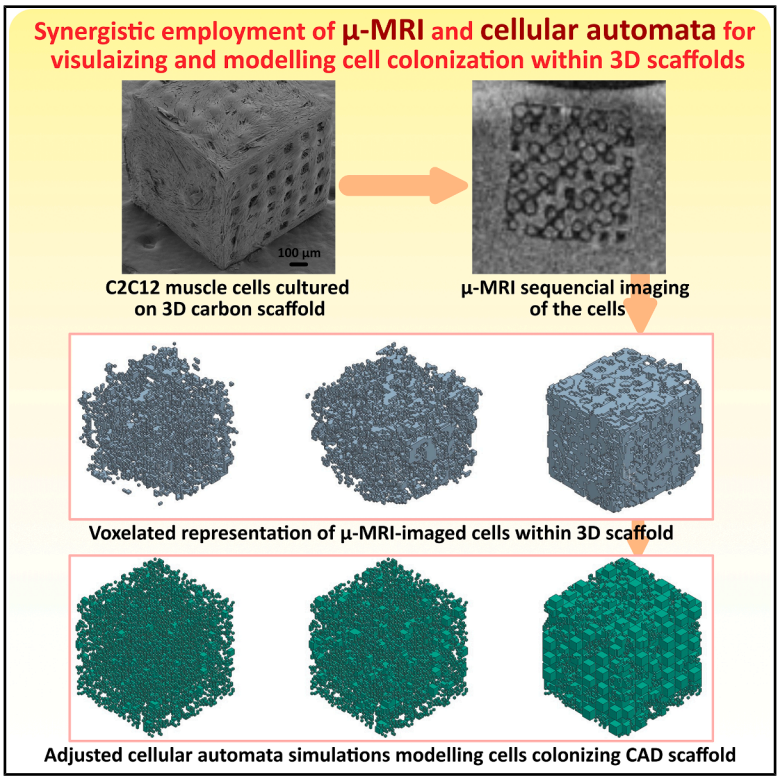

Highlights

- A methodology for seeing and modeling cells within biomaterials is presented and evaluated
- Visualization of cells within scaffolds is enabled by magnetic resonance microscopy
- Carbon scaffolds are used as biomaterials compatible with magnetic resonance microscopy
- Cellular automata are employed for modeling cells colonizing the scaffolds

Authors

Andrés Díaz Lantada, Mazin Jouda, William Solórzano-Requejo, Dario Mager, Monsur Islam, Jan Gerrit Korvink

Correspondence

andres.diaz@upm.es (A.D.L.), monsurislam79@gmail.com (M.I.), jan.korvink@kit.edu (J.G.K.)

In brief

Díaz Lantada and colleagues present a methodology for visualizing cells within biomaterials or scaffolds and modeling their colonization. Magnetic resonance microscopy using carbon scaffolds is synergically employed with cellular automata for seeing and simulating the cells, which constitutes an innovative technological combination for tissue engineering, biofabrication, and engineered living materials.

Díaz Lantada et al., 2025, Cell Reports Physical Science 6, 102629
June 18, 2025
https://doi.org/10.1016/j.xcrp.2025.102629

CellPress

Cell Reports
Physical Science

CellPress
OPEN ACCESS

Article

Combining μ-MRI with cellular automata simulation for an improved insight into cell growth within scaffolds

Andrés Díaz Lantada,[1,4,*] Mazin Jouda,[2] William Solórzano-Requejo,[1] Dario Mager,[2] Monsur Islam,[3,*] and Jan Gerrit Korvink[2,*]

[1]Mechanical Engineering Department, ETSI Industriales, Universidad Politécnica de Madrid, Calle José Gutiérrez Abascal 2, 28006 Madrid, Spain

[2]Institute of Microstructure Technology, Karlsruhe Institute of Technology, Hermann von Helmholtz Platz 1, 76344 Eggenstein Leopoldshafen, Germany

[3]IMDEA Materials Institute, Calle Eric Kandel 2, 28906 Getafe, Spain

[4]Lead contact

*Correspondence: andres.diaz@upm.es (A.D.L.), monsurislam79@gmail.com (M.I.), jan.korvink@kit.edu (J.G.K.)

https://doi.org/10.1016/j.xcrp.2025.102629

SUMMARY

Tissue engineering scaffolds are pivotal for modern healthcare research. However, studying cell-cell and cell-material interactions within these scaffolding networks is time consuming and technically demanding. In most cases, the cells within the scaffolds are not visible to classical imaging technologies, so what happens within remains unknown. An emerging non-destructive option for studying cells within scaffolds is micro-magnetic resonance imaging (μ-MRI). In this research, its applications to imaging cells within tissue engineering scaffolds during different periods and quantifying colonization processes within pyrolytic carbon networks for their special physical-chemical properties are explored and discussed. Additionally, toward resource-efficient tissue engineering, *in silico* approaches are raising the attention of the research community. These simulations can be performed employing cellular automata interacting with computer-aided design (CAD) models, which mimic cell colonization of scaffolds. Our study demonstrates that μ-MRI proves a remarkable technology for fine-tuning these computational models.

INTRODUCTION

Biohybrid materials, in which living cells and abiotic materials coexist or cooperate, are already proving transformative in healthcare, being central to fields like tissue engineering and biofabrication.[1–3] Many of these evolve from the classical tissue engineering concept, in which a synthetic extracellular matrix or scaffold is populated by eukaryotic cells and functionalized with chemokines and cytokines to achieve an advanced medicinal therapy product.[4–6] Apart from the therapeutic applications of scaffolds with cells to repair damaged tissues or reconstruct biological structures, their employment for drug screening applications, supporting diagnosis, and predicting the evolution of disease is also extremely remarkable.[7,8]

As cell culture processes are resource and time consuming, the combination of *in vitro* studies, culturing cells within biomimetic scaffolds, and *in silico* approaches, which are capable of modeling cell-cell and cell-material interactions, has gained attention in recent years. In fact, the term "*in silico* tissue engineering" is quite recent and heralds a future of digital twins applied to cellular therapies.[9,10] These *in silico* strategies, adequately fine-tuned with experimental data, can allow for more efficient, sustainable, and ethical biomedical research and align with the 3R (replace, reduce, and refine) principles[11,12] that aim to minimize animal testing. Various computational models, both continuous and discrete,[13–15] enable the simulation of collective cellular behaviors, in connection with challenges linked to the modeling of pathologies and therapeutic strategies and to the engineering of biomedical devices, especially lab-on-a-chip microsystems and scaffolds.[16–19] Typically, discrete models simulate cell colonies in environments that emulate Petri dish cultures. However, research in the field of "labs on a chip" and "organs on a chip" demonstrates that the information obtained in 2D cultures using Petri dishes differs from the fidelity of results achievable when using more biomimetic microfluidic environments to model pathological processes and associated therapies. In 3D microenvironments, the situation is even more complex, as shown by research in the field of tissue scaffolds, which are used to both model pathological processes *in vitro* and reconstruct defects, and in tissue engineering in general. Lately, cellular automata and hybrid cellular automata finite-element methods have been proposed for modeling tissue engineering and cancer treatment,[20–22] although their experimental adjustment and validation are challenging.

Indeed, in the case of studying cell-cell and cell-material interactions *in vitro* within tissue engineering scaffolds or when aiming at validating *in silico* tissue engineering and *in silico*

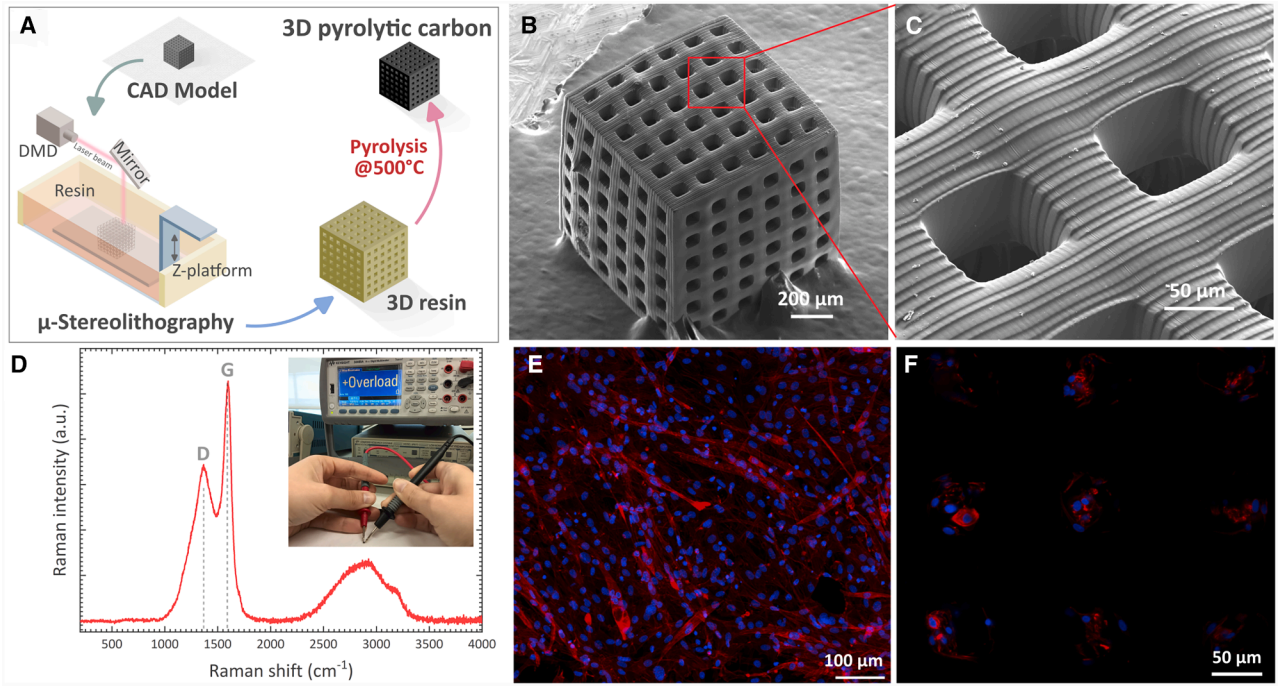

Figure 1. 3D-printed PyC microlattice scaffolds for C2C12 cells

(A) Schematic illustration of the fabrication process of 3D PyC scaffold.

(B) Low-magnification SEM image of 3D PyC scaffold depicting its shape retention after pyrolysis. Scale bar: 200 μm.

(C) High-magnification SEM image of the PyC scaffold showing the microstructural features of the 3D scaffold. Scale bar: 50 μm.

(D) Raman spectra of the PyC material. The inset shows the electrical resistance reading through a digital multimeter, depicting the electrical inertness of the fabricated carbon scaffold.

(E) Maximum-intensity projection of fluorescence images of C2C12 muscle cells cultured on a 3D PyC scaffold after 7 days of culture. The nucleus was stained with Hoechst (blue), and actin fibers were stained with phalloidin (red). Scale bar: 100 μm.

(F) The cultured muscle cells within the pores of the 3D scaffold, signifying the proliferation of the cells within the 3D environment of the scaffold. Scale bar: 50 μm.

disease progression models, seeing cells in three dimensions constitutes a fundamental challenge. Normally, cells upon the surfaces of scaffolds are visualized using optical, fluorescent, confocal, or electronic microscopy, which, in some cases, permits 3D representations of cells and scaffolds but is not capable of exploring the inner regions of intricate biohybrid constructs.[23] Alternatives include cryo-sectioning and microtome,[24,25] which are destructive, and microcomputed tomography (μ-CT), which is non-destructive but employs ionizing radiation with potentially harmful effects for the cells and tissues under study.[26] Besides, μ-CT cannot recapitulate cellular dynamics, microfluidic interactions, thermal phenomena, and diffusion processes, for which magnetic resonance imaging (MRI) is more suitable.[27,28]

In our driving hypothesis, micro-MRI (μ-MRI) may emerge as a facilitating technology for the characterization and optimization of tissue engineering scaffolds and biohybrid materials in general due to its unique feature of non-destructive live monitoring capable of exploring the diffusion of nutrients, hormones, and drugs, the flow through vascular structures, and even the metabolic state of tissues and organs.

Furthermore, by achieving single-cell resolution, longitudinal studies of scaffold colonization by cells could be applied to the adjustment of *in silico* tissue engineering models.

In addition, to image the cells in a 3D microenvironment, pyrolytic carbon (PyC) scaffolds are proposed. 3D features can be controlled from the design stage, as they are computationally designed and manufactured through a combination of stereolithographic photopolymerization and subsequent pyrolysis. Furthermore, the pyrolysis process results in significant geometrical shrinkage, allowing the geometrical features of the PyC scaffold to reach a geometrical scale comparable to the cell size, which is otherwise extremely challenging in other manufacturing processes. PyC material is also found to be transparent to μ-MRI signals, which should facilitate cell visualization and quantification tasks.

To demonstrate our hypothesis and illustrate the potentials of μ-MRI for studying scaffolds with cells and biohybrid systems, we take inspiration from the pioneering study of Fuhrer et al.,[29] in which stochastic cellular scaffolds of glassy carbon were used for culturing neural cells and μ-MRI allowed for the visualization of neural cell clusters. Following that pioneering study, this study presents important breakthroughs: first, cells cultured upon PyC scaffolds during different periods are evaluated with μ-MRI to perform a quasi-longitudinal study of cell colonization. Second, cellular resolution is achieved by employing a special imaging setup and visualization procedure, which is demonstrated by comparing the 3D reconstructions of the scaffolds

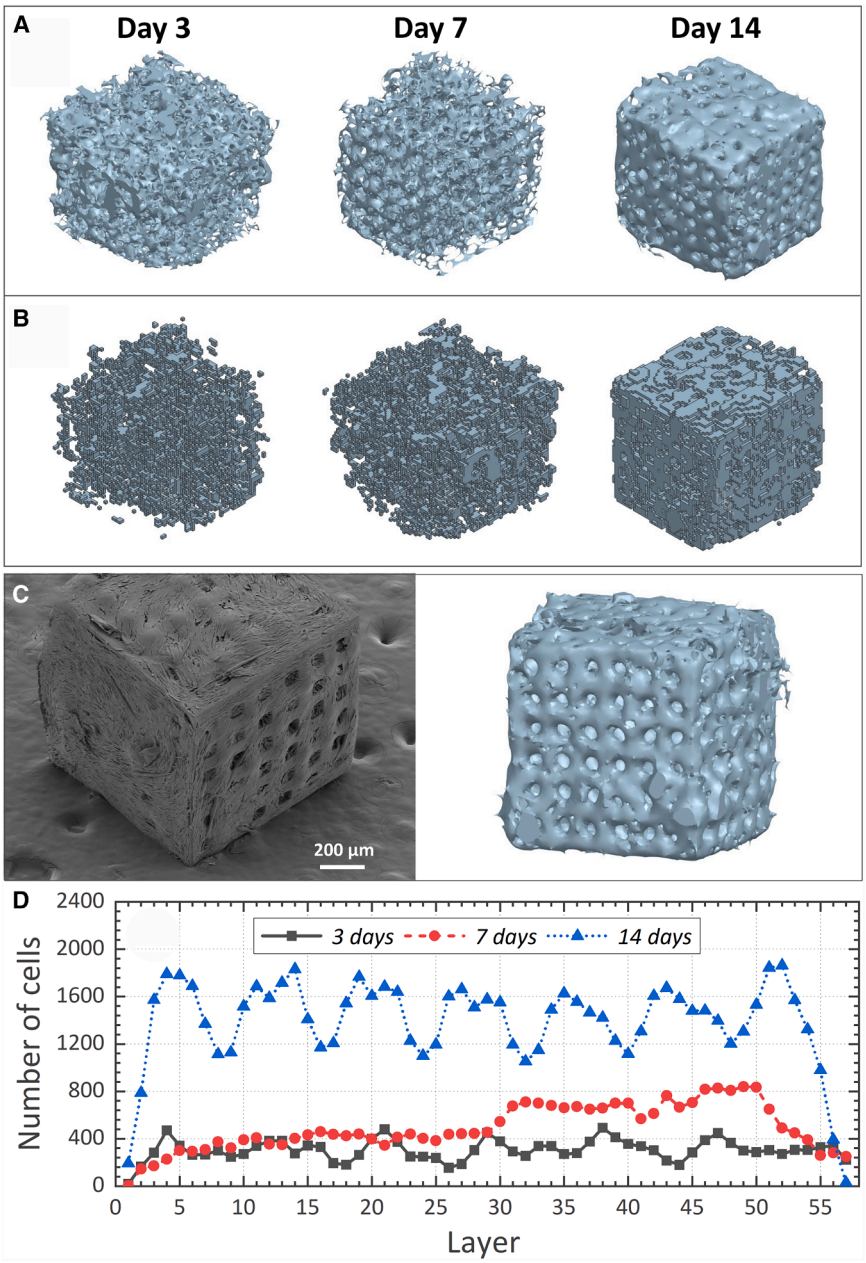

Figure 2. 3D reconstruction of µ-MRI imaged cells within 3D PyC scaffolds

(A) Results from 3D reconstructions: different views from cells colonizing carbon scaffolds after 3 (left), 7 (middle), and 14 (right) days of cell culture.

(B) Corresponding voxelated representations of the cells for subsequent adjustment of cellular automata simulations.

(C) Comparative view of the 3D reconstruction after µ-MRI (.stl file, right) and scanning electron microscopy (SEM; left) for the 14 day culture, demonstrating the possibility of achieving cellular resolution with µ-MRI. Scale bar: 200 µm.

(D) Cell numbers quantified by voxel counting across the scaffold layers and depending on culture time.

with cells obtained from the µ-MRI files with scanning electron microscopy (SEM) images. Third, the cellular colonization of scaffolds is quantitatively evaluated by measuring the volume and surface of reconstructed computer-aided design (CAD) models in stereolithographic (or standard tessellation language [stl]) file formats. Fourth, the quantification obtained from µ-MRI files is employed to adjust a simulation of cellular automata, operating within the boundaries of a tissue engineering scaffold CAD model, which simulates cells colonizing scaffolds.

The presented strategy constitutes an innovative methodology for evaluating cells within biomaterials and fine-tuning agent-based models simulating biohybrid constructs and their evolution, as shown in the results below and further discussed.

RESULTS

Manufacturing of PyC scaffolds and cell culture results

Designed scaffolds of 3D PyC material were successfully fabricated using micro-stereolithography of a precursor resin, followed by high-temperature pyrolysis, as described in the methods section. The 3D PyC material retained the designed cubic lattice geometry, as illustrated by the SEM images of the PyC materials (Figure 1B). The pyrolysis-associated shrinkage process led to a PyC lattice thickness of 80.2 ± 2.7 µm, with a gap between the lattices of 83.9 ± 5.9 µm. This translated to shrinkages of 46.6% ± 1.8% in the lattice thickness and 44.0% ± 3.9% in the pore size. Notably, the lattice thickness and pore dimension of 3D PyC scaffolds are comparable to the size of the muscle cells and the resolution of the µ-MRI system. The high-magnification SEM image of the PyC scaffold (Figure 1C) further revealed the printing lines in the scaffold, which could further facilitate cell attachment and alignment during culture, an important factor for muscle cell growth.

To evaluate the material characteristics of the PyC material, we performed Raman spectroscopy. The Raman spectrum of the 3D PyC material is presented in Figure 1D, which features two prominent peaks around 1,360 and 1,596 cm^{-1}, typical characteristics of carbon materials.[30] The peak around 1,360 cm^{-1}, assigned as the D-peak, signifies the disorder in the carbon matrix, whereas the peak around 1,596 cm^{-1}, denoted as the G-peak, corresponds to the graphitic order of carbon. Typically, a lower intensity ratio between the D-peak and G-peak is considered to be the highly graphitic nature of the carbon material. For instance, pure graphite features an intensity ratio of zero.[31]

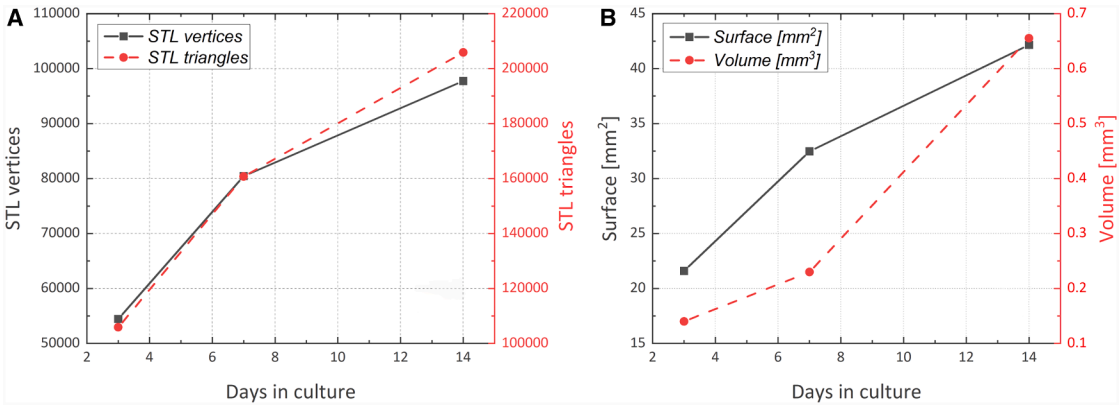

Figure 3. Quantification based on reconstructed and voxelated .stl files

(A) Number of elements (triangles in the tessellation) and vertices versus culture time in days in the original .stl files.

(B) Surface and volume as a function of days in culture, quantified after voxelization.

Our PyC material exhibited an intensity ratio of 0.7. However, the pyrolysis process for our PyC material was performed at 500°C, which was significantly low for generating graphitic carbon. It has been proven from several *in situ* experimental studies and molecular dynamic simulations that during pyrolysis of an organic precursor, the graphitic carbon starts to form above a temperature of 700°C.[32–34] Below this temperature, the carbon remains mainly in an amorphous state. We believe that despite having a lower D/G ratio, our PyC material was also highly amorphous. The significantly higher area ratio of D- and G-peaks (A_D/A_G = 2.26), as obtained from the deconvolution of the Raman spectrum, supports the amorphous behavior of our PyC material. The low-intensity and non-pronounced 2D band around 2,800 cm^{-1} further aids in proving the presence of high defect densities. Furthermore, the obtained PyC exhibited an overloading of electrical resistance while measured using a digital multimeter (inset of Figure 1D), suggesting its electrical insulating nature. Such characteristics are well in agreement with already published reports on carbon materials obtained from low-temperature pyrolysis.[35–37]

As reported in our previous article, PyC scaffolds are biocompatible and able to host cells, inducing good proliferation and cell growth.[38] Following the published work, we cultured C2C12 muscle cells on the fabricated PyC microlattice scaffold as the model cells in our study.

Figure 1E presents a representative maximum-intensity projection of the fluorescence image of the cultured cells on a PyC scaffold, highlighting the phalloidin-stained actin fibers (red) and Hoechst-stained nuclei (blue). The actin fibers seemed to be distributed in the cytoskeleton on the PyC surface, suggesting the formation of monolayers on the PyC surface. Sequential imaging of the cells further revealed the growth of the cells within the pores of the scaffold, as shown in Figure 1F.

μ-MRI at cellular scale

Non-destructive characterizations of the scaffolds with cells, employing μ-MRI as described in the methods section, were performed. Once the .dicom (digital communications in medicine) files were obtained, 3D Slicer was employed as open medical imaging visualization software to process the files, segment them according to the adequate thresholds of Hounsfield's scale for soft tissues, and generate the .stl files for qualitative and quantitative evaluation of imaging results. Subsequent voxelization enables the quantitative comparison with agent-based simulations and the fine-tuning of the cellular automata modeling scaffold colonization processes. Random cell clusters out of the boundaries of the scaffolds were discarded, and the volumetric limits of the PyC scaffolds were subsequently employed as limiting boundaries for the cellular automata simulations. The PyC scaffolds, as expected, prove transparent to μ-MRI, which facilitates a focus on cellular colonization and a quantification taking into consideration just the cells. This also helps with the fine-tuning of the cellular automata simulations by counting voxels with cells in state 2 (the presence of a cell within the scaffold boundaries defined by CAD). The PyC scaffolds withstand the imaging procedure, which helps to verify the non-destructive nature of the procedure.

Considering the imaging results, Figure 2 presents a selection of images resulting from the first study and reconstruction using the high-resolution mode of the μ-MRI system. These images correspond to reconstructed cell cultures visualized for different pyrolytic scaffolds but cultured in the same conditions and fixed at different moments (3, 7, and 14 days). In this way, a quasi-longitudinal scaffold colonization study was achieved, as the same scaffold was not monitored during different timelines; rather, three scaffolds cultured in similar conditions were studied for three different periods. Figure 2A includes different views of the colonized scaffolds, Figure 2B presents the voxelated cells after the postprocessing of three-dimensionally reconstructed images, and Figure 2C includes a comparative view of the 3D reconstruction after μ-MR imaging (.stl file, Figure 2C, right) and SEM (Figure 2C, left). In the .stl reconstructions, cells are depicted in blue, and the different images and views show the cells progressively forming a continuous biofilm upon the carbon scaffolds, which are completely colonized by the cells. This is also appreciated in the SEM image, and even concrete cell clusters can be univocally seen both in the reconstructed structures after μ-MRI and in the SEM employed as a gold standard for imaging the

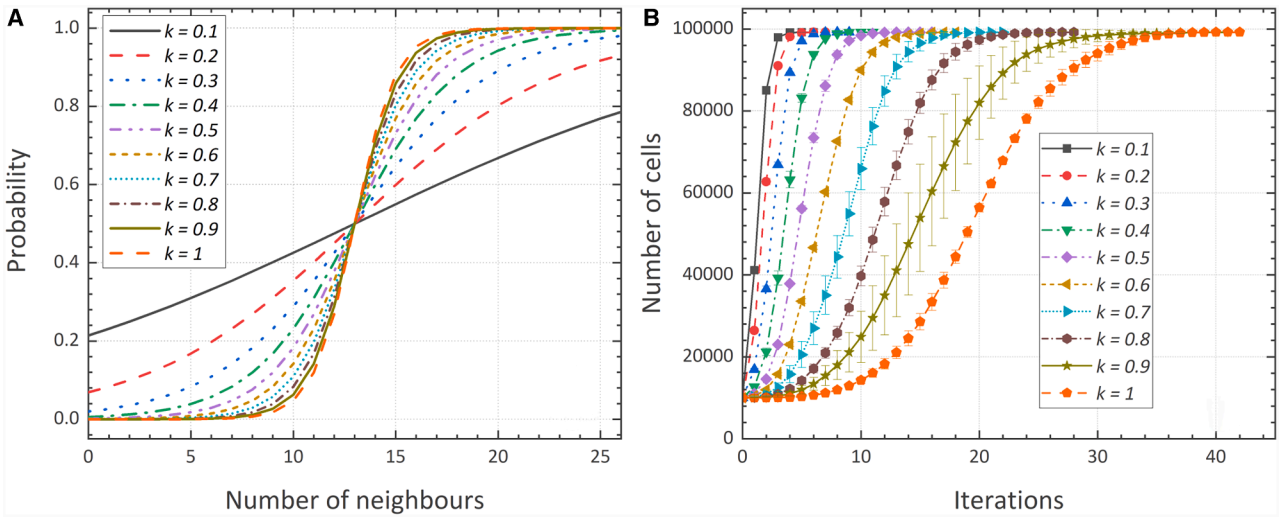

Figure 4. Influence of sigmoid parameter k

Probability function (A) and number of cells per iteration (B) by varying k in sigmoid equation.

external regions. In short, cell morphologies can be perceived both in the μ-MRI reconstructions and in the SEM image.

The different views presented show that scaffolds cultured for shorter periods yielded larger pores, which were not yet filled with cells. The pore size became smaller as the culture time increased, and the biofilms became more compact and thicker. This illustrates the possibility of monitoring cell populations growing within biomaterials using μ-MRI. Another important result is that the cells and the PyC scaffolds were good companions for these non-destructive evaluations. Although in this study, the different scaffolds are fixed at different moments, the inspiring study by Fuhrer and colleagues[29] verified the possibility of *in vivo* monitoring of cell clusters within μ-MRI systems. Among the advantages of μ-MRI, it is necessary to point out that the reconstructed geometries can be freely rotated, expanded, and sliced, all of which are interesting for the visualization of the inner regions of the scaffolds. Indeed, this allows for the quantification of cells (by voxel counting) across the layers of the different scaffolds, as shown in Figure 2D. Internal visualization is not possible with other classical imaging resources, and μ-MRI stands out as a non-destructive and minimally invasive resource. Some cell clusters are visualized both with μ-MRI and SEM, and the fact that similar topographies are found with both technologies, corresponding to cellular features, demonstrates the possibility of reaching the cellular scale, which had been previously reported in other studies.[29,39]

Once obtained, the .stl reconstructions of 3D cell cultures were employed for additional quantification purposes. The quantification results are presented in Figure 3. While Figure 3A illustrates the number of elements (triangles in the tessellation) and vertices versus culture time in days in the original .stl files, Figure 3B deals with cellular surface and volume as a function of days in culture, quantified after voxelization. As expected, the volume evolution exhibited a monotonically increasing function during the cell culture period, which corresponded to a population of healthy cells in culture populating the scaffolds. Interestingly, both the .slt file size and the number of elements and measured exposed surface increased more rapidly at the beginning.

To the authors' understanding, considering the limitations of the study described in the methods section and the discussion, this corresponded to the progressive achievement of a more compact and homogeneous biofilm along the colonization. Initially, cells were more scattered, and the thickness of the biofilm was more irregular. With time, the fractured aspect of the biofilm (and the corresponding fractal dimension) decreased, leading to a more conformal cell coating and a reduction of the surface-to-volume ratio.

Application to adjusting cell colonization simulations

The cellular automaton described in the methods is defined by a probabilistic rule based on the sigmoid equation (Equation 1), which depends on parameters "k" and "c." The calibration of these parameters is performed in two steps: in the first, k is varied by keeping c at a fixed value of 13, and in the second, c is varied using the best value of k previously obtained. To compare all simulations, a MATLAB code was developed that converts iterations into days using a conversion factor. This code tests different factors and selects the one that minimizes the mean absolute error (MAE) when comparing the number of simulated cells with the experimental ones (μ-MRI).

Figure 4 shows the probability functions when varying k from 0.1 to 1 in intervals of 0.1 and how the number of cells evolves with iterations. We observe that the value of c (in this case, 13) regulates the point where the probability is 0.5 and that varying k alters the slope of the sigmoid, making it steeper at higher values. Lower values of k increase the probability of cell growth even with few neighbors in state 2 and slightly decrease the probability of growth with many live neighbors, as can be seen in Figure 5. Simulations show that with low k, the number of iterations to colonize the entire scaffold is lower compared to higher k values. The MAE analysis comparing the experimental outcomes with the mean number of cells obtained with the cellular

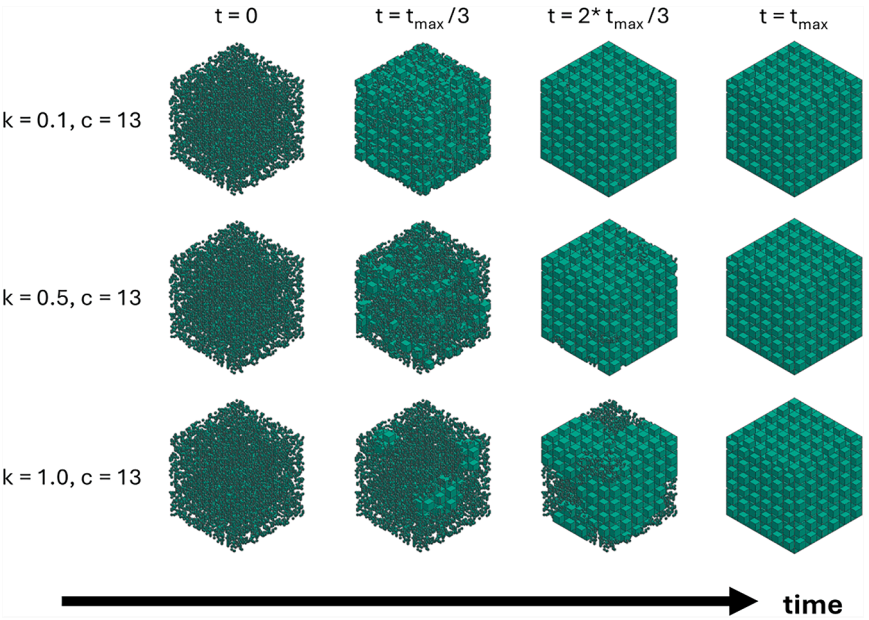

Figure 5. Cellular automaton evolution by varying k in the sigmoid equation

Cellular automaton evolution by varying k in the sigmoid equation.

automaton suggests that the lowest error is obtained with a k of 0.4 (Table S1), so the next step is to keep k at that value and vary c progressively.

Figure 6 shows the probability functions when varying c from 4 to 22 in intervals of 3, thus changing the probability point by 0.5. Lower values of c make cell growth with few neighbors more likely, which accelerates scaffold colonization. Starting from the initial assumption of 10,000 randomly distributed cells on the scaffold, favoring growth with few neighbors speeds up the process, as there will be more and more cells, and due to the nature of the sigmoid, the probability of growth with more neighbors will also increase. This effect on c is also reflected in the evolution of the cellular automaton observed in Figure 7. Analyzing the mean MAE (Table S2), the simulation with k = 0.4 and c = 13 is still the best, with a scale factor of 2.9, indicating that one iteration represents approximately 2.9 days of experimentation. Therefore, the simulation suggests that full colonization of the scaffold will occur in 32 days, reaching 95% of the cells within the scaffold in approximately 17 days.

By graphically comparing the best simulation with the experimental data, first applying the scaling factor to convert iterations to days (Figure 8A), and overlaying the plots (Figure 8B), it follows that days 7 and 14 correlate very well and that the MAE of 1,911.19 is mainly due to the error on day 3. Furthermore, comparing the voxelated representations of the cells in the PyC scaffolds with the simulations shows that the complex growth patterns that the automaton can generate with a simple probabilistic rule closely resemble the real ones (see Figure 9 and .gif animations provided in Data S1).

DISCUSSION

The adjusted cellular automata adequately represent the cellular colonization of a tissue engineering scaffold, both qualitatively and quantitatively, as shown in Figure 8 and further illustrated in Figure 9. The utility of the simulations includes the possibility of performing interpolations and, to some extent, extrapolations of the evolving biohybrid system, without requiring continuous monitoring of the experiment, just by validating the simulation with a low number of imaging experiments.

By tuning the adjustment parameters, the temporal resolution of the simulation can predict intermediate states among planned measurements and contribute to quality controls. In addition, apart from quantitative data on expectable cell numbers and distributions, other interesting quantities, like the surface-to-volume ratio of the growing biological construct, can be forecasted, as shown in Figure 10. The decreasing value indicates a more conformal biofilm being formed and can provide an indication of the health state of the whole biohybrid system. It is worth mentioning that the behavior of the 3D cellular automaton is very similar to cell growth in a Petri dish. Therefore, the cellular automaton can simulate the lag, stationary, and exponential growth phases of the cells, although our model does not yet consider the death phase due to cell overpopulation. To include this phase, one could explore the use of an automaton with memory that penalizes a cell that has been alive for many iterations.

Fluidic accessibility could also be taken into account in connection with access to nutrients or exposure to applied drugs. This could, for example, be implemented with an overlayed gradient field that would modify the probabilities of the cellular automata according to nutrition or drug exposure, among others. This penalty would be associated with a probability of death, depending on the discrete time a cell has been alive, thus improving the accuracy of the simulation in high-cell-density scenarios. With increased cellular states, the effect of drugs and the interactions among cell types could be modeled,[40] while the influence of physical/chemical fields on cellular behaviors could be simulated by employing hybrid finite-element cellular automata approaches.[41]

The main limitation of the study is linked to the visualization of fixed cells cultured for different periods in a set of tissue engineering scaffolds. Although the cell culture conditions and the scaffolding geometries employed were the same for the different samples, the colonization study performed was not a longitudinal study illustrating how cells continuously grow and populate a concrete synthetic extracellular matrix. However, it constituted a preliminary approach to analyze the technological viability of visualizing with cellular resolution, reconstructing cellular morphologies and colonies within a 3D environment, and simulating them within the scaffolding structure.

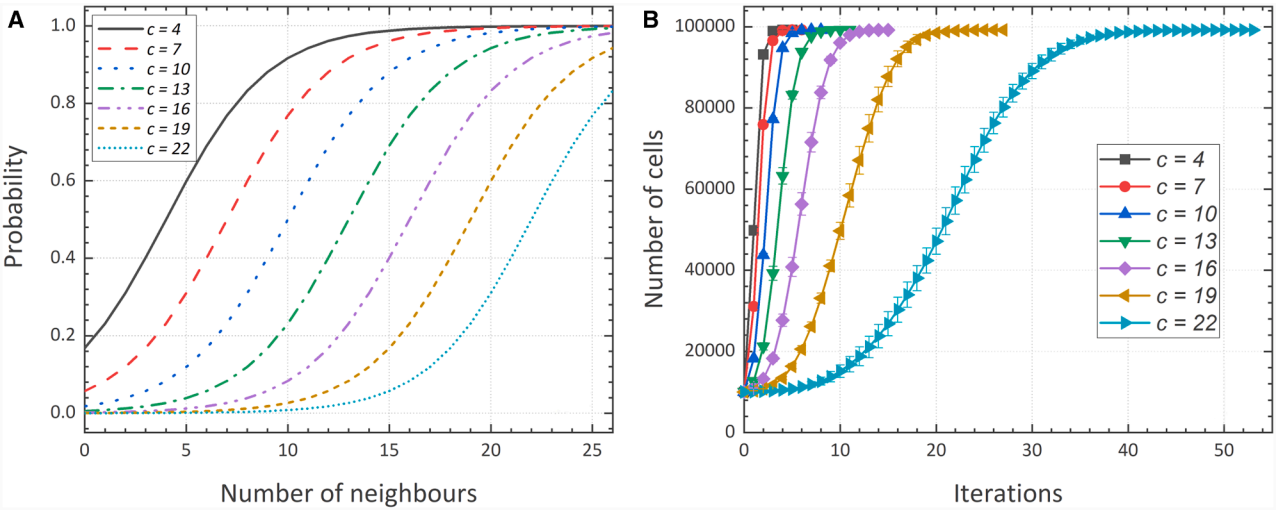

Figure 6. Influence of sigmoid parameter c

Probability function (A) and number of cells per iteration (B) by varying c in the sigmoid equation.

Furthermore, the simulations performed have been developed with important simplifications, like the use of an initial homogeneous distribution of cells, the omission of the possible influences of nutrients or drugs, and the lack of modulating fields, for instance obtained from finite-element simulations, to better recapitulate mechanobiological and biochemical cues. Only two states for the empty voxels of the grid have been employed here (1 for the absence of cells and 2 for the presence of cells, with state 0 being the voxels occupied by the scaffolding structure). Different metabolic states and various cellular populations interacting within the scaffolds, which can be visualized with μ-MRI, would need an increased number of possible states for the fine-tuning of more realistic simulations.

Notwithstanding the above, among interesting results, the adequate partnership between cells and PyC scaffolds for performing these studies and the possibility of jointly employing μ-MRI, .stl reconstructions based on .dicom files for quantification purposes, and agent-based simulations fine-tuned with imaging results have been demonstrated. These open up a plethora of innovative research directions, as explained below.

Toward the future, counting with a microfluidic setup for *in vivo* studying cells during several days in culture within the μ-MRI system would help us achieve true longitudinal colonization periods with living cells imaged daily or weekly.

Besides, culturing other cell types and studying different cells and their mutual interactions within scaffolds of different materials would be another interesting research direction. In previous studies, we verified the usability of osteoblast-like murine cells (MC3T3) in PyC scaffolds, visualized employing fluorescence microscopy. In this study, we wanted to explore a musculoskeletal cell line because of the potential of PyC scaffolds as future chassis for biohybrid micromachines, as recently put forward.[38] We wanted to explore the interactions of this cell line and its compatibility with the PyC scaffolds, but we wanted a cell line that would still be more robust and user friendly than human mesenchymal stem cells, whose μ-MRI visualization will be explored in the future. Furthermore, considering that μ-MRI responds to the diffusion of nutrients, hormones, and drugs, the flow through vascular structures, and even the metabolic state of tissues and organs, several applications emerge by combining cells cultured within PyC scaffolds and imaged using magnetic resonance. Among these, the study of angiogenesis, the monitoring of cancer progression, and a better understanding of metastatic processes can be mentioned. Some of these have been extensively simulated with cellular automata and hybrid cellular automata finite-element models, whose experimental validation is often challenging or inviable using traditional imaging techniques. The possibility of imaging at cellular resolution and discriminating among cells and tissues using μ-MRI and experimental methods similar to those presented here can lead to significant healthcare applications. Pioneering studies in the field will expectedly allow us to analyze more complex cellular environments and behaviors.[42]

Beyond healthcare, the methods illustrated can be applied to any kind of bioprinted constructs and biohybrid materials in general in connection with the emergent field of engineered living materials (ELMs), in which different living cells and abiotic materials coexist or cooperate. These ELMs are already proving transformative in a wide set of fields, including energy production, materials processing, industrial recycling, and even micro/nanorobotics. A new challenge is perceived here, as many living materials involve prokaryotic cell colonies, either as part of biohybrid constructs or in the form of cultured biofilms. To the authors' best knowledge, μ-MRI has not yet been employed for monitoring bacteria and archaea within synthetic scaffolds or biomaterial constructs. Although we foresee that prokaryotes will be even more complex to visualize and individualize by employing μ-MRI due to their smaller size when compared to eukaryotic cells, technological advances in the hardware and software of these imaging systems make us confident about their technical viability.

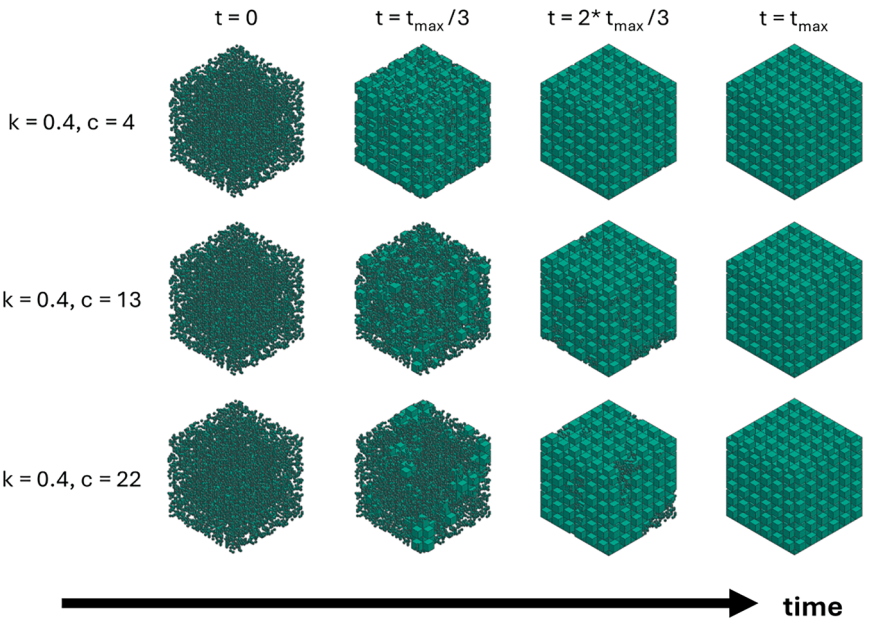

Figure 7. Cellular automaton evolution by varying c in the sigmoid equation

Cellular automaton evolution by varying c in the sigmoid equation.

In summary, cells within scaffolds are challenging to see, and the ways they colonize porous biomaterials are complex to monitor with classical imaging resources. According to the presented results, μ-MRI can help solve these issues, allowing for the inspection of tissue engineering scaffolds, thus achieving cellular resolution. PyC scaffolds constitute a remarkable platform for performing these *in vitro* cell culture and imaging studies due to their remarkable biocompatibility and their lack of response to nuclear magnetic resonance. Potentials for performing quantitative evaluations of longitudinal scaffold colonization processes and adjusting agent-based simulations that mimic the behavior of cells within extracellular matrices have been analyzed.

The experimental methodology employed by our team opens new horizons, not only for characterizing tissue engineering scaffolds with cells but also for several types of bioprinted constructs, ELMs, and biohybrid systems in general.

To the authors' best understanding, the combined application of μ-MRI and cellular automata has been studied and validated in this study for the first time. Their synergies are remarkable: μ-MRI results help to experimentally adjust the cellular automata simulations, while these can support quantitative predictions, interpolations, and extrapolations aimed at more efficiently employing the imaging resources.

METHODS

Fabrication of 3D PyC scaffold and characterization

The fabrication process is schematically illustrated in Figure 1A. We chose 3D microlattice structures with cubic unit cells as the scaffold structure. The structures, featuring a regular lattice with a rod thickness of 150 μm and unit cell dimension of 300 μm, leaving a gap between adjacent rods of 150 μm, were designed using SolidWorks, a CAD software developed by Dassault Systèmes. The CAD design is illustrated in Figure 1A. The designed structures were subsequently additively manufactured using the Boston Micro Fabrication (BMF) MicroArch S130 laser micro-stereolithography machine while using a commercial epoxy resin from BMF (HTL yellow resin) as the photopolymerizable precursor and a layer thickness of 5 μm during printing. Once the printing was finished, the printed structures were washed in isopropyl alcohol for 15 min to remove any excess uncured resin, followed by further curing for 1 h inside a UV chamber.

We carbonized the 3D-printed epoxy structures in a horizontal tube furnace (Nabertherm, Germany) under constant nitrogen gas flow (flow rate: 80 L/h) to convert the structures to 3D PyC. The heat treatment protocol used here is often used by our group for pyrolytic conversion of organic precursors. Briefly, the temperature of the furnace was ramped to 350°C with a heating ramp of 3°C/min, followed by isothermal heating at 350°C for 3 h to remove excess oxygen from the heating tube. After that, the temperature was further increased to 500°C with a heating rate of 3°C/min, followed by another isothermal heating step at 500°C for 2 h to ensure complete carbonization. The furnace was finally cooled down to room temperature using natural cooling under ongoing gas flow. 3D PyC scaffolds were characterized for their microstructure and dimensions using SEM (Apreo 2S LoVac, Thermo Fisher Scientific). Furthermore, we performed Raman spectroscopy of the PyC materials using a Renishaw inVia micro-Raman spectrometer with a laser wavelength of 532 nm (2.33 eV).

Cell culture

We used skeletal muscle cells (C2C12) as the model cells in our study. The cells were cultured in a low-endotoxin Dulbecco's modification of Eagle medium, supplemented with 10% fetal bovine serum (PAN-biotech, Germany), 1% penicillin/streptomycin (Sigma-Aldrich, Germany), and 4.5 g/L glucose (PAN-biotech, Germany) under growth conditions of 37°C, 5% CO_2, at about 90% humidity. Before contact with the cells, the 3D PyC scaffolds were disinfected by immersing them in 70% ethanol for 1 h at room temperature. The scaffolds were thoroughly washed in 1× Dulbecco's balanced salt solution (DPBS) (Sigma-Aldrich), followed by incubation in a culture medium for 2 h in similar incubation conditions. The cell seeding within the PyC scaffold was performed in 35 mm glass-bottom dishes (ibidi, Germany) with a concentration of 10,000 cells per dish. The cell culture was continued for a maximum period of 14 days, with the renewal of fresh media every 2–3 days. For

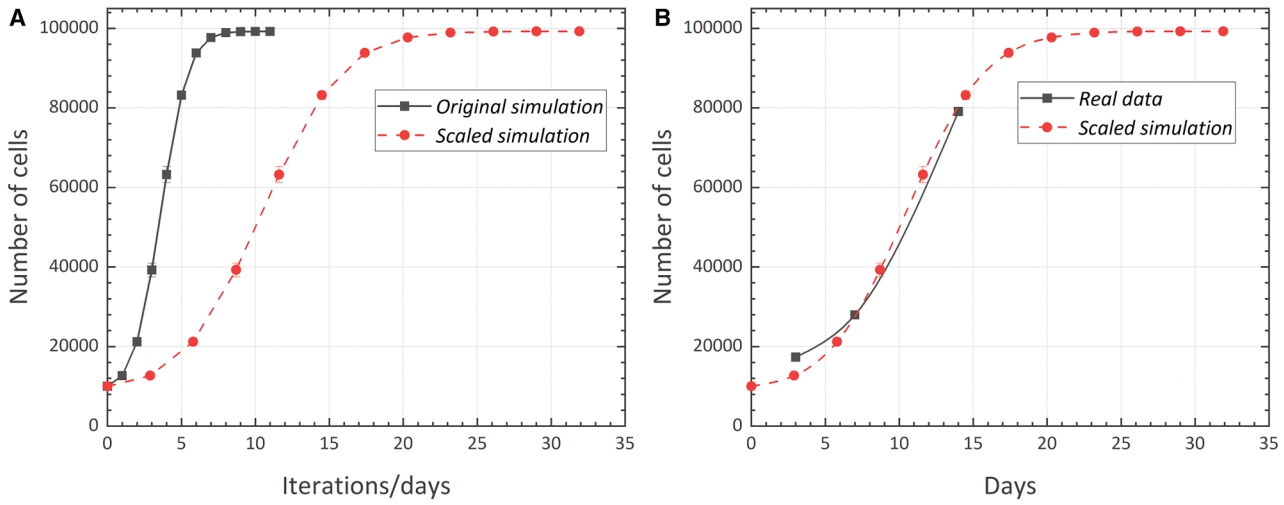

Figure 8. Comparison of cell numbers in experiments and simulations

(A) Number of cells obtained from the cellular automata simulations as a function of iterations or days.

(B) Comparison between the number of cells per day of the simulation and the cell culture experiment by measuring the number of voxels after voxelated .stl generation from μ-MRI.

studying the intermediate growth of the cells, selected cell cultures were stopped at 3, 7, and 14 days and processed with a cell fixation step using 4% paraformaldehyde (Sigma, Germany) for 1 h at room temperature.

For imaging of the cultured cells, a cell staining protocol was followed. The cells were first treated with 0.2% Triton X-100 (Sigma) in DPBS for 10 min at room temperature to allow permeabilization, followed by a thorough rinse in DPBS. To block non-specific binding, the samples were then incubated for 1 h in a blocking solution made up of 3% w/v bovine serum albumin (Sigma-Aldrich), 0.1% Tween 20 (Sigma-Aldrich), and 10% fetal bovine serum. To label actin within the muscle cells, Alexa Fluor 647 phalloidin (Invitrogen, USA) was used at a 1:1,000 dilution in the blocking solution, also for 1 h at room temperature. Following another wash with 0.1% Tween 20 in DPBS, the samples were treated with Hoechst 33258 (Invitrogen) at a concentration of 10 μg/mL in the blocking solution for 20 min at room temperature and then washed again. The confocal imaging was carried out with a confocal microscope (Nikon AX).

μ-MRI

The magnetic resonance microimaging experiments were conducted on a wide-bore Bruker AVANCE NEO system operating at a field strength of 11.7 T, corresponding to a 1H Larmor frequency of 500 MHz. A 5 mm saddle coil and a micro-imaging gradient were utilized. The samples were placed in a 5 mm glass tube filled with buffer solution. The micro-imaging parameters were as follows: a 3D gradient-echo sequence (GRE) with a flip angle (FA) of 45°, a receiver bandwidth (BW) of 50 kHz, an echo time (TE) of 4.3 ms, and a repetition time (TR) of 70 ms. The matrix size was 300 × 300 × 150, with 18 acquisitions (NEX), resulting in a total scan time of 15 h and 45 min. The field of view (FoV) was 6 × 6 × 3 mm, yielding an isotropic resolution of 20 μm. The isotropic resolution matches the cell size and is also considered for the voxelization of the reconstructed images and for defining the voxel size for performing and adequately adjusting the cellular automata simulations.

Supporting characterization resources and methods

Once obtained, .dicom files resulting from μ-MRI were processed employing 3D Slicer (https://github.com/Slicer/Slicer), which is a "free, open-source software for visualization, processing, segmentation, registration, and analysis of medical, biomedical, and other 3D images and meshes; and planning and navigating image-guided procedures" widely used by the research community and originally developed by Fedorov et al.[43] For segmentation and reconstruction purposes, a threshold was applied to select Hounsfield's scale values between 4 and 59, with the intention of visualizing soft matter and considering that PyC is transparent to MRI. Once segmented and transformed into .stl files, measuring options of common CAD software and .stl visualization programs were applied to obtain appropriate quantification. For comparative purposes, SEM (JEOL JSM-7610F) was performed upon selected scaffolds using a 5 kV electron beam. Prior to SEM, the cell-seeded scaffolds were coated with 5 nm titanium and 15 nm gold, respectively, using a sputtering system (MED 020, Bal-Tec, Germany).

Cellular automata simulation of cells colonizing scaffolds

From the segmented scaffolds, a cellular automaton model can be developed and calibrated to simulate their colonization, following previous experiences by our team,[40,41,44] with some important modifications. The cellular automaton is represented by a grid of cells, where each cell has a state, an interaction neighborhood, and a rule that determines the

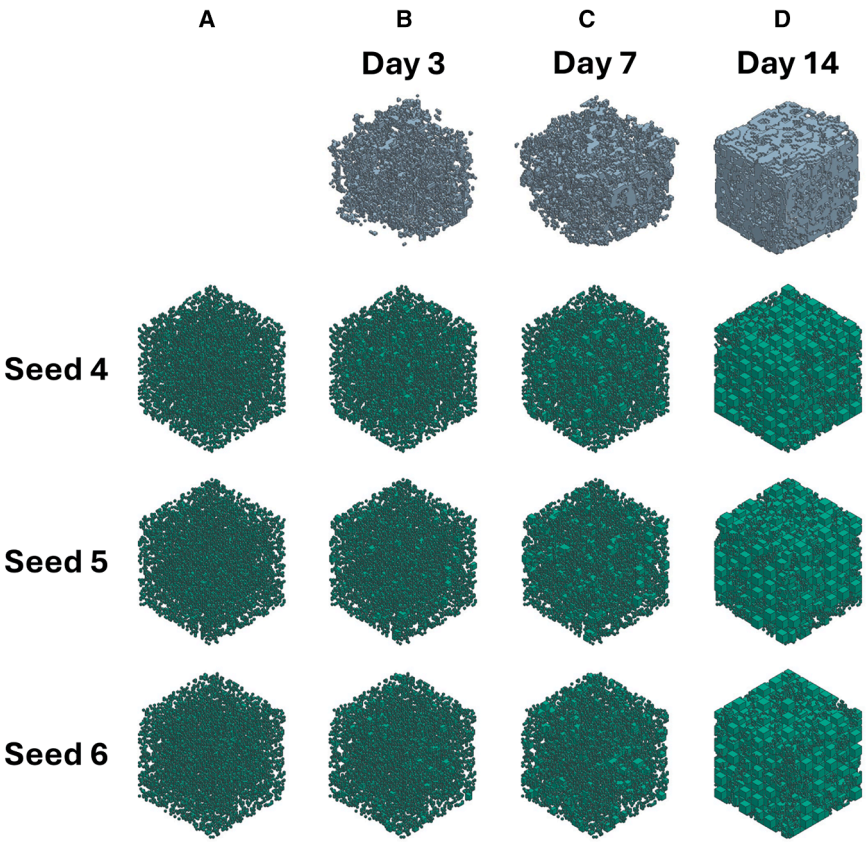

Figure 9. Comparative representation of initial and cultured cell states

(A) Initial state with 10,000 cells.

(B–D) Comparison between simulations (green) and experiments (blue) at 3 (B), 7 (C), and 14 (D) days. Simulations were performed with different random seeds.

system dynamics in a deterministic or probabilistic manner. The rule is based on the state of the cell under analysis and those of its neighbors.

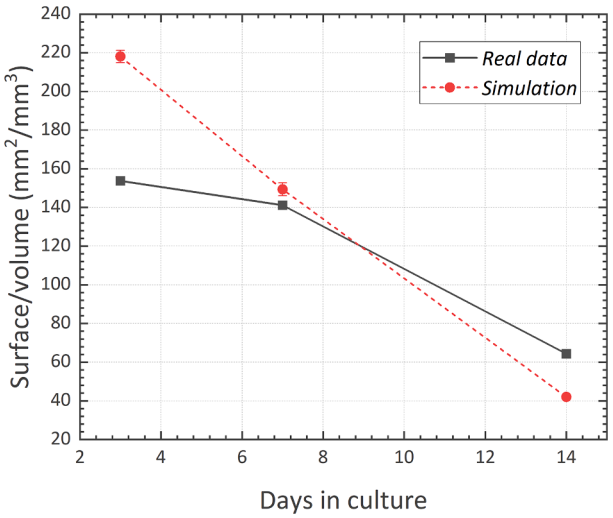

Figure 10. Simulated and experimentally measured surface-to-volume ratio versus days in culture

Simulated and experimentally measured surface-to-volume ratio versus days in culture.

For the implementation of the cellular automaton, MATLAB R2023b (The Mathworks) was used. The grid of cells represents the PyC scaffold. To obtain its virtual model, the CAD file of the scaffold is scaled down to 60% to simulate the volumetric shrinkage due to pyrolysis. This file is then imported into CHITUBOX v.1.9.5 (Chitubox, Zhongcheng Future Industrial Park, Hangcheng Avenue, Baoan District, Shenzhen, Guangdong 518128, China), a software for resin 3D printers that generates digital masks similar to the images from MRI slices. In this software, the voxel resolution was set to $20 \times 20 \times 20\ \mu m^3$, hence taking into consideration both the real cell size and the imaging resolution. From these images, the scaffold can be reconstructed in MATLAB, and each part of the cellular automaton can be defined. All the images were imported into MATLAB and binarized, and their negative version was obtained to highlight the inner part of the scaffold, which corresponds to the space where the cells grow, defined by state 1, while the scaffold is defined as state 0. The next step is to identify the voxels adjacent to the inner surfaces of the scaffold, from which 10,000 will be randomly selected, which corresponds to the 10,000 cells per dish cited in the cell culture methods. This is done to start the cell ingrowth process, defining them as the first cells to adhere to the scaffold (state 2, which means the presence of living cells).

In the cellular automaton simulation, whose code is available in Zenodo (see resource availability), each voxel of the structure is processed from left to right and from bottom to top. If a cell has a state equal to 1, it is analyzed and evaluated to determine whether it will change state in the next iteration. A 3D Moore neighborhood is defined, which considers all cells adjacent to the cell under analysis as neighbors, resulting in a total of 26 neighbors. A probabilistic rule is defined for the change of state from 1 to 2, based on a sigmoid function (Equation 1) that determines the probability of change according to the number of neighbors in state 2. The sigmoid has two parameters, k and c, whose values are calibrated experimentally to find those that best model the dynamics of the system.

$$\text{prob} = \frac{1}{1+e^{-k \cdot (\text{number of Moore neighbors} - c)}} \quad \text{(Equation 1)}$$

To update the state of the cell under analysis, the number of neighbors in state 2 is counted, and the probability of change is calculated using the sigmoid equation. This value is compared with a pseudo-random number generated with the MATLAB command "rand." If the probability is higher, the cell state changes; otherwise, it remains in the current state. To ensure the reproducibility of the cellular automata simulations, three different random seeds (4, 5, and 6) are used to incorporate experimental variability. A random seed is a number that initializes a pseudo-random number generator and ensures consistency across simulations. A predefined seed is used in each run, and at each iteration, the number of growing cells is quantified and compared with experimental results.

RESOURCE AVAILABILITY

Lead contact

Further information and requests for resources and reagents should be directed to and will be fulfilled by the lead contact, Andrés Díaz Lantada (andres.diaz@upm.es).

Materials availability

All materials generated in this study are available from the lead contact with a completed materials transfer agreement.

Data and code availability

- All relevant data are included in the paper.
- The code for simulating the cellular automata colonizing PyC scaffolds is shared openly in Zenodo at https://doi.org/10.5281/zenodo.15260115.
- Any additional information required to reanalyze the data reported in this paper is available from the lead contact upon request.

ACKNOWLEDGMENTS

The authors acknowledge support from the Deutsche Forschungsgemeinschaft (DFG, German Research Foundation) under Germany's Excellence Strategy via the Excellence Cluster "3D Matter Made to Order" (EXC-2082/1–390761711). J.G.K. acknowledges project support from the ERC Synergy Grant HiSCORE (951459). The authors acknowledge the support of researchers Barbara Schamberger, Mohammadreza Taale, and Christine Selhuber-Unkel, from the Institute for Molecular Systems Engineering and Advanced Materials (IMSEAM) at Heidelberg University, for their support with culturing cells. A.D.L. acknowledges the funding from the Spanish Ministry of Universities (senior researcher mobility project PRX21/00460) that sponsored his research stay at KIT during spring-summer 2022 and acknowledges the Karlsruhe Institute of Technology for supporting him with an "International Excellence Fellowship" for his research at KIT during spring-summer 2023.

AUTHOR CONTRIBUTIONS

Conceptualization, A.D.L., D.M., M.I., and J.G.K.; imaging experiments and image processing, A.D.L., M.J., M.I., and W.S.-R.; design and prototyping, A.D.L. and M.I.; simulations, W.S.-R.; data analysis and discussion of results, all co-authors; writing – original draft, A.D.L., W.S.-R., and M.I.; writing – review & editing, M.J., D.M., and J.G.K.; resources, A.D.L. and J.G.K.; supervision, A.D.L., M.I., and J.G.K.

DECLARATION OF INTERESTS

J.G.K. is a shareholder of Voxalytic GmbH, a company that produces and sells MRI and NMR probe heads, which did not affect the objective presentation of results.

SUPPLEMENTAL INFORMATION

Supplemental information can be found online at https://doi.org/10.1016/j.xcrp.2025.102629.

Received: December 6, 2024
Revised: April 7, 2025
Accepted: May 15, 2025
Published: June 10, 2025

REFERENCES

1. Wang, C., Zhang, Z., Wang, J., Wang, Q., and Shang, L. (2022). Biohybrid materials: Structure design and biomedical applications. Mater. Today Bio *16*, 100352.
2. Ruiz-Hitzky, E., and Wicklein, B. (2018). The fascinating world of the functional hybrid and biohybrid materials. Adv. Funct. Mater. *28*, 1803407.
3. Smith, R.S.H., Bader, C., Sharma, S., Kolb, D., Tang, T., Hosny, A., Moser, F., Weaver, J.C., Voigt, C.A., and Oxman, N. (2020). Hybrid living materials: digital design and fabrication of 3D multimaterial structures with programmable biohybrid surfaces. Adv. Funct. Mater. *30*, 1907401.
4. Langer, R., and Vacanti, J. (2016). Advances in tissue engineering. J. Pediatr. Surg. *51*, 8–12.
5. Hutmacher, D.W. (2000). Scaffolds in tissue engineering bone and cartilage. Biomaterials *21*, 2529–2543.
6. Hutmacher, D.W., Sittinger, M., and Risbud, M.V. (2004). Scaffold-based tissue engineering: rationale for computer-aided design and solid free-form fabrication systems. Trends Biotechnol. *22*, 354–362.
7. Marei, I., Abu Samaan, T., Al-Quradaghi, M.A., Farah, A.A., Mahmud, S.H., Ding, H., and Triggle, C.R. (2022). 3D tissue-engineered vascular drug screening platforms: promise and considerations. Front. Cardiovasc. Med. *9*, 847554.
8. Kankala, R.K., Zhang, Y.S., Kang, L., and Ambrosio, L. (2023). Editorial: Polymeric microarchitectures for tissue regeneration and drug screening. Front. Bioeng. Biotechnol. *11*, 1144991.
9. Makarov, D.E. (2021). Life in silico: Are we close yet? Proc. Natl. Acad. Sci. USA *118*, e2100278118.
10. Geris, L., Lambrechts, T., Carlier, A., and Papantoniou, I. (2018). The future is digital: In silico tissue engineering. Curr. Opin. Biomed. Eng. *6*, 92–98.
11. Hubrecht, R.C., and Carter, E. (2019). The 3Rs and Humane Experimental Technique: Implementing Change. Animals *9*, 754.
12. Jean-Quartier, C., Jeanquartier, F., Jurisica, I., and Holzinger, A. (2018). In silico cancer research towards 3R. BMC Cancer *18*, 408.
13. Jarrett, A.M., Lima, E.A.B.F., Hormuth, D.A., 2nd, McKenna, M.T., Feng, X., Ekrut, D.A., Resende, A.C.M., Brock, A., and Yankeelov, T.E. (2018). Mathematical models of tumor cell proliferation: a review of the literature. Expert Rev. Anticancer Ther. *18*, 1271–1286.
14. Torii, R., Velliou, R.-I., Hodgson, D., and Mudera, V. (2018). Modelling multi-scale cell–tissue interaction of tissue-engineered muscle constructs. J. Tissue Eng. *9*, 2041731418787141.
15. Krause, A.L., Beliaev, D., Van Gorder, R.A., and Waters, S.L. (2019). Lattice and continuum modelling of a bioactive porous tissue scaffold. Math. Med. Biol. *36*, 325–360.
16. Post, J.N., Loerakker, S., Merks, R.M.H., and Carlier, A. (2022). Implementing computational modeling in tissue engineering: Where Disciplines Meet. Tissue Eng. Part A *28*, 542–554.
17. Yang, Q., Ju, D., Liu, Y., Lv, X., Xiao, Z., Gao, B., Song, F., and Xu, F. (2021). Design of organ-on-a-chip to improve cell capture efficiency. Int. J. Mech. Sci. *209*, 106705.
18. Garijo, N., Manzano, R., Osta, R., and Perez, M.A. (2012). Stochastic cellular automata model of cell migration, proliferation and differentiation: Validation with in vitro cultures of muscle satellite cells. J. Theor. Biol. *314*, 1–9.

19. Vivas, J., Garzón-Alvarado, D., and Cerrolaza, M. (2015). Modeling cell adhesion and proliferation: a cellular-automata based approach. Adv. Model. Simul. Eng. Sci. *2*, 32.

20. Czarnecki, J.S., Jolivet, S., Blackmore, M.E., Lafdi, K., and Tsonis, P.A. (2014). Cellular automata simulation of osteoblast growth on microfibrous-carbon-based scaffolds. Tissue Eng. Part A *20*, 3176–3188.

21. Insua, A. M. 2015 Tumor growth analysis using cellular automata.

22. Messina, L., Ferraro, R., Peláez, M.J., Wang, Z., Cristini, V., Dogra, P., and Caserta, S. (2023). Hybrid cellular automata modeling reveals the effects of glucose gradients on tumour spheroid growth. Cancers (Basel) *15*, 5660.

23. Leferink, A.M., van Blitterswijk, C.A., and Moroni, L. (2016). Methods of monitoring cell fate and tissue growth in three-dimensional scaffold-based strategies for in vitro tissue engineering. Tissue Eng. Part B Rev. *22*, 265–283.

24. Thevenot, P., Nair, A., Dey, J., Yang, J., and Tang, L. (2008). Method to analyze three-dimensional cell distribution and infiltration in degradable scaffolds. Tissue Eng. Part C Methods *14*, 319–331.

25. Fuchs, J., Mueller, M., Daxböck, C., Stückler, M., Lang, I., Leitinger, G., Bock, E., El-Heliebi, A., Moser, G., Glasmacher, B., and Brislinger, D. (2019). Histological processing of un-/cellularized thermosensitive electrospun scaffolds. Histochem. Cell Biol. *151*, 343–356.

26. Petruzzellis, F., Pagliarani, C., Savi, T., Losso, A., Cavalletto, S., Tromba, G., Dullin, C., Bär, A., Ganthaler, A., Miotto, A., et al. (2018). The pitfalls of in vivo imaging techniques: evidence for cellular damage caused by synchrotron X-ray computed micro-tomography. New Phytol. *220*, 104–110.

27. Badilita, V., Meier, R.C., Spengler, N., Wallrabe, U., Utz, M., and Korvink, J. G. (2012). Microscale nuclear magnetic resonance: a tool for soft matter research. Soft Matter *8*, 10583–10597.

28. Hertig, D., Maddah, S., Memedovski, R., Kurth, S., Moreno, A., Pennestri, M., Felser, A., Nuoffer, J.M., and Vermathen, P. (2021). Live monitoring of cellular metabolism and mitochondrial respiration in 3D cell culture system using NMR spectroscopy. Analyst *146*, 4326–4339.

29. Fuhrer, E., Bäcker, A., Kraft, S., Gruhl, F.J., Kirsch, M., MacKinnon, N., Korvink, J.G., and Sharma, S. (2018). 3D carbon scaffolds for neural stem cell culture and magnetic resonance imaging. Adv. Healthc. Mater. *7*, 1700915.

30. Thapliyal, V., Alabdulkarim, M.E., Whelan, D.R., Mainali, B., and Maxwell, J.L. (2022). A concise review of the Raman spectra of carbon allotropes. Diam. Relat. Mater. *127*, 109180. https://doi.org/10.1016/j.diamond.2022.109180.

31. Ferrari, A.C. (2007). Raman spectroscopy of graphene and graphite: Disorder, electron–phonon coupling, doping and nonadiabatic effects. Solid State Commun. *143*, 47–57. https://doi.org/10.1016/j.ssc.2007.03.052.

32. Montgomery-Walsh, R., Nimbalkar, S., Bunnell, J., Galindo, S.L., and Kassegne, S. (2021). Molecular dynamics simulation of evolution of nanostructures and functional groups in glassy carbon under pyrolysis. Carbon N. Y. *184*, 627–640. https://doi.org/10.1016/j.carbon.2021.08.070.

33. Sharma, S., Shyam Kumar, C.N., Korvink, J.G., and Kübel, C. (2018). Evolution of Glassy Carbon Microstructure: In Situ Transmission Electron Microscopy of the Pyrolysis Process. Sci. Rep. *8*, 16282. https://doi.org/10.1038/s41598-018-34644-9.

34. Eggeler, Y.M., Chan, K.C., Sun, Q., Díaz Lantada, A., Mager, D., Schwaiger, R., Gumbsch, P., Schröder, R., Wenzel, W., Korvink, J.G., and Islam, M. (2024). A Review on 3D Architected Pyrolytic Carbon Produced by Additive Micro/Nanomanufacturing. Adv. Funct. Mater. *34*, 2302068. https://doi.org/10.1002/adfm.202302068.

35. Schuepfer, D.B., Badaczewski, F., Guerra-Castro, J.M., Hofmann, D.M., Heiliger, C., Smarsly, B., and Klar, P.J. (2020). Assessing the structural properties of graphitic and non-graphitic carbons by Raman spectroscopy. Carbon *161*, 359–372. https://doi.org/10.1016/j.carbon.2019.12.094.

36. Islam, M., Weidler, P.G., Heissler, S., Mager, D., and Korvink, J.G. (2020). Facile template-free synthesis of multifunctional 3D cellular carbon from edible rice paper. RSC Adv. *10*, 16616–16628. https://doi.org/10.1039/D0RA01447H.

37. Jurkiewicz, K., Pawlyta, M., Zygadło, D., Chrobak, D., Duber, S., Wrzalik, R., Ratuszna, A., and Burian, A. (2018). Evolution of glassy carbon under heat treatment: correlation structure–mechanical properties. J. Mater. Sci. *53*, 3509–3523. https://doi.org/10.1007/s10853-017-1753-7.

38. Taale, M., Schamberger, B., Monclus, M.A., Dolle, C., Taheri, F., Mager, D., Eggeler, Y.M., Korvink, J.G., Molina-Aldareguia, J.M., Selhuber-Unkel, C., et al. (2024). Microarchitected compliant scaffolds of pyrolytic carbon for 3D muscle cell growth. Adv. Healthc. Mater. *13*, e2303485. https://doi.org/10.1002/adhm.202303485.

39. van Schadewijk, R., Krug, J.R., Shen, D., Sankar Gupta, K.B.S., Vergeldt, F.J., Bisseling, T., Webb, A.G., Van As, H., Velders, A.H., de Groot, H.J.M., and Alia, A. (2020). Magnetic resonance microscopy at cellular resolution and localised spectroscopy of Medicago truncatula at 22.3 Tesla. Sci. Rep. *10*, 971.

40. Ballesteros Hernando, J., Ramos Gómez, M., and Díaz Lantada, A. (2019). Modeling living cells within microfluidic systems using cellular automata models. Sci. Rep. *9*, 14886.

41. Díaz Lantada, A., Sánchez, M., and Fernández, D. (2023). In silico tissue engineering and cancer treatment using cellular automata and hybrid cellular automata-finite element models. In 16th International Conference on Biomedical Electronics and Devices, pp. 56–63. https://doi.org/10.5220/0011742300003414.

42. Korvink, J.G., MacKinnon, N., Badilita, V., and Jouda, M. (2019). "Small is beautiful" in NMR. J. Magn. Reson. *306*, 112–117.

43. Fedorov, A., Beichel, R., Kalpathy-Cramer, J., Finet, J., Fillion-Robin, J.C., Pujol, S., Bauer, C., Jennings, D., Fennessy, F., Sonka, M., et al. (2012). 3D Slicer as an image computing platform for the Quantitative Imaging Network. Magn. Reson. Imaging *30*, 1323–1341.

44. Solórzano-Requejo, W., Aguilar, C., Callejo, G., and Díaz Lantada, A. (2024). Biodegradable Biodevices: A Design Approach Based on Cellular Automaton. In 17th International Conference on Biomedical Electronics and Devices, pp. 34–41. https://doi.org/10.5220/0012313600003657.